Journal of Materials Chemistry A

Accepted Manuscript

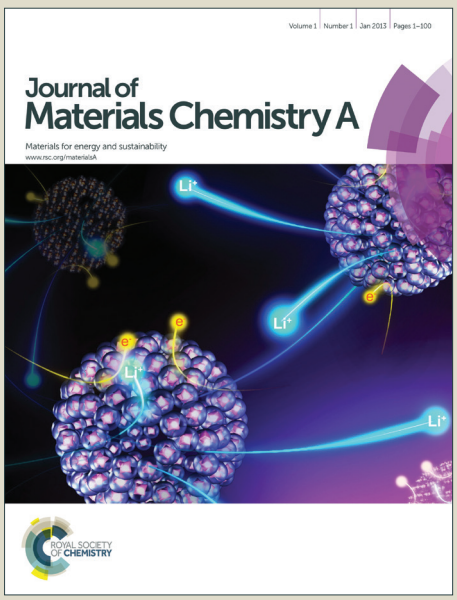

ROYAL SOCIETY OF CHEMISTRY

www.rsc.org/materialsA

Journal of Materials Chemistry A

RSCPublishing

ARTICLE

Cation ordering in *A*-site-deficient Li-ion conducting perovskites $La_{(1-x)/3}Li_xNbO_3$

Cite this: DOI: 10.1039/x0xx00000x

Received 00th December 2014,
Accepted 00th XXX XXXX

DOI: 10.1039/x0xx00000x

www.rsc.org/

Xiang Gao,*[a] Craig A. J. Fisher,[a] Yumi H. Ikuhara,[a] Yasuyuki Fujiwara,[b] Shunsuke Kobayashi,[a] Hiroki Moriwake,[a] Akihide Kuwabara,[a] Keigo Hoshikawa,[b] Keiichi Kohama,[c] Hideki Iba[c] and Yuichi Ikuhara*[ad]

Cation-deficient perovskites exhibit complex local atomic arrangements which cannot be adequately described by average crystal structure models. By combining reciprocal-space electron diffraction analysis and direct observations of atom positions using state-of-the-art scanning transmission electron microscopy, we clarify the nature of the cation ordering within *A*-site-deficient perovskite single crystals of $La_{(1-x)/3}Li_xNbO_3$ (x = 0 and x = 0.04). Both materials are found to have complex modulated crystal structures with two types of *A*-cation ordering, namely a long-range layer ordering in alternate $(001)_p$ planes and a short-range (intra-domain) columnar ordering within La-rich $(001)_p$ layers. The columnar ordering (occupational modulation) produces modulated displacements of Nb and O atoms. It is also found that substitution of even a small amount of Li for La can affect significantly the columnar ordering, leading to a series of structural and microstructural changes that are likely to have a deleterious effect on the Li-ion conductivity of this material.

1. Introduction

A-site-deficient perovskites A_xBO_3 (x < 1) represent a large group of materials which usually have complex superstructures containing ordered arrangements of *A* cations and vacancies, giving rise to a range of interesting dielectric, photocatalytic, magnetic, and electrochemical properties.[1] In particular, $RE_yLi_xBO_3$ perovskites, where the *A* site is occupied by a rare earth (*RE*) and lithium, so that $x + y < 1$, and *B* = Ti or Nb, and their derivatives are very attractive not only because of their high Li-ion conductivity, making them suitable for a number of applications such as electrochemical sensors and secondary Li-ion and Li-air batteries, but also as model materials for fundamental investigations of solid-state ionic diffusion and electrochemical reactions in complex oxides.[2-13] In these materials, the distribution of *RE* cations over *A* sites determines the pathways available for Li-ion migration, as well as the size of bottlenecks along the pathways formed between vertex-sharing BO_6 octahedra.[14,15] The distribution of *RE* ions is thus a critical factor affecting the overall ionic conductivity.

X-ray diffraction (XRD) and neutron diffraction (ND) studies have revealed that the *RE* atoms in $RE_yLi_xBO_3$ are invariably partitioned into alternating vacancy-poor (A1) and vacancy-rich (A2) layers parallel to $(001)_p$ (where the subscript "p" refers to the primitive perovskite unit cell).[3-7,9-11] End members such as $Th_{0.33}NbO_3$ and $La_{0.33}NbO_3$ (LNO) have crystal structures with two-thirds of *A* sites occupied by *RE* atoms in the A1 layer (vacancy-poor layer) and all A cages empty in the A2 (vacancy-rich) layer, as illustrated in Fig. 1.[16-18] This long-range ordering (primary ordering) of *A* cations is accompanied by displacement of the transition-metal cations on

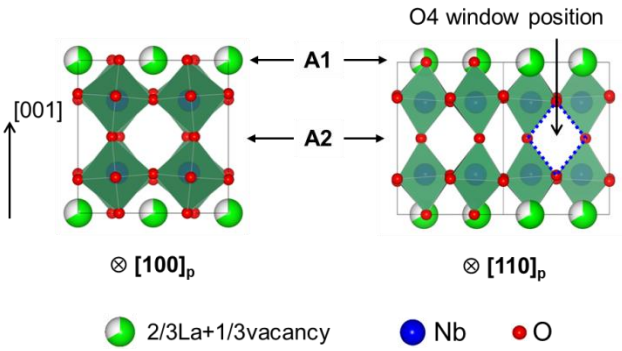

Fig. 1 Average crystal structure model. Projections of the *A*-site deficient $La_{(1-x)/3}Li_xNbO_3$ (x = 0) perovskite network down $[100]_p$ (left) and $[110]_p$ (right) directions reveal the partially occupied (A1) and unoccupied (A2) *A*-cation layers. "p" refers to the primitive perovskite structure.

the *B* sites from the centres of their octahedra to the underbonded oxide ions in the vacancy-rich $(001)_p$ layers as a result of a second-order Jahn-Teller distortion. This distortion relieves the bonding instability caused by layer ordering,[19] and results in a decrease of crystal symmetry from cubic to tetragonal or orthorhombic (depending on the Li concentration) with a doubling of the *c* parameter.

The structural complexity of *A*-site-deficient perovskites means that they are still poorly understood, despite intense interest.[20] Previous studies have shown that these materials produce complex satellite reflections in selected area electron diffraction (SAED) patterns.[16,17,21-24] However, the origin of these reflections is still a matter of controversy. Various interpretations have been suggested, including formation of nanodomains,[20] microdomains,[16,21-23] unidentified sub-superstructures,[17] and the combined effects of crystal structure modulation, octahedral tilting, structural vacancies, and/or the formation of microdomains.[24-26] One feature these explanations have in common is that the local structures in these perovskites can deviate greatly from the average structures derived from XRD and ND measurements. In the case of $RE_yLi_xNbO_3$ materials the SAED superlattice reflections are in the form of diffusion rods,[16,21,24] indicative of the presence of modulated crystal structures. Up until now the nature of these modulated structures has not yet been reported in any detail, however.

The lack of such information means that the relationship between the crystal structure of $La_{(1-x)/3}Li_xNbO_3$ (LLNO) and its electrochemical properties is still being debated. Compared to $La_{(2-x)/3}Li_xTiO_3$ (LLTO), LLNO perovskites have a larger unit cell volume, a smaller concentration of La^{3+} ions and a higher concentration of intrinsic vacancies; the latter are expected to favour higher Li-ion mobility and hence higher ionic conductivity.[27] However, this is not what is experimentally observed. Electrochemical measurements show that LLNO compounds have a maximum bulk ionic conductivity at room temperature of about 10^{-4} Scm^{-1} when $x = 0.195$,[9] which is an order of magnitude smaller than that of LLTO for its optimum composition of $x = 0.29$.[4,28] On the other hand, an earlier XRD study of LLNO ascribed the changes in ionic conductivity with increasing Li content to changes in the lattice parameters.[29] Measurement of the variation in interatomic distances in different LLNO compounds using the extended x-ray absorption fine structure (EXAFS) technique suggests the average structural changes obtained from XRD are not adequate for explaining the changes in Li-ion conductivity, which is determined by the local atomic structure.[30] This implies that the local structural changes can be more varied than those inferred from macro-scale measurements; detailed characterization is thus needed to elucidate and optimise the ionic conductivity in LLNO materials.

Conventional transmission electron microscopy (TEM) methods, such as SAED and HREM, have proven useful for studying superstructures in complex perovskites. Until recently, a method for probing local configurations with atomic resolution, particularly in the case of weakly-scattering light elements like Li ($Z = 3$, where Z is atomic number), has not been available. However, recent advances in aberration-corrected STEM have largely overcome this problem. The annular bright field (ABF) imaging method, which produces absorption signals roughly proportional to $Z^{1/3}$, enables columns of both light and heavy atoms over a wide range of specimen thicknesses to be characterized simultaneously with unprecedented accuracy.[31,32] This technique has been used to image Li atoms in various crystalline electrode and electrolyte materials in real space and real time.[15,33-36] It can also be used simultaneously with high-angle annular dark-field (HAADF) imaging, whose signals scale roughly in proportion to $Z^{1.7}$. In addition, recent improvements in monochromator technology now make it possible to perform electron energy-loss spectroscopy (EELS) analysis with high energy resolution so that even slight variations of the local chemical and electronic states can be probed. When integrated with a scanning transmission electron microscope, these state-of-the-art methods provide a powerful toolkit for exploring local atomic configurations, even in the case of very complex microstructures such as those encountered in many Li-ion battery materials. Recent examples include observation of local clustering of *A* cations and vacancies,[15] as well as characterisation of domain boundaries in solid electrolyte LLTO,[33] interface structures in $LiMn_2O_4$/Au,[35] and $LiCoO_2/Al_2O_3$ cathodic thin film systems.[36,37]

To elucidate the relationship between microstructure and the electrochemical properties of this family of materials, single-crystalline samples of two different LLNO compositions were prepared: an Li-free sample, $La_{0.33}NbO_3$ (LNO), and a low-Li-content sample of composition $La_{0.32}Li_{0.04}NbO_3$ (LLNO4). Here we report the results of direct observation of the crystal structures of these perovskites with atomic resolution using HAADF/ABF imaging and monochromated EELS analysis. The origin of the SAED satelli2te reflections, the effect of Li substitution on crystal structure modulation, as well as the possible influence of cation ordering on Li-ion mobility, are discussed in the following section.

2. Experimental

2.1. Materials processing

Perovskite single crystals $La_{(1-x)/3}Li_xNbO_3$ with compositions x = 0 and 0.04 were grown by a unidirectional solidification method.[39] Raw materials were prepared by a conventional solid-state reaction using Li_2CO_3 (99.9%), La_2O_3 (99.9%) and Nb_2O_5 (99.9%) as starting materials. Mixtures of the starting materials was calcined at 700 ℃ for 2.5 h in air. Calcined powders were ground, compacted and fired again at 1200 ℃ for 12 h in air. They were sintered into cylinders of dimensions 20 mm diameter, and 50 to 60 mm length, giving a density of 3.8 to 4.1 g/cm^3, for single crystal growth. Each sample was placed in a platinum crucible (20 mm inner diameter × 150 mm height × 0.12 thickness) and heated from room temperature to 1380 ℃ at a rate of 30 ℃/min in air in a conventional unidirectional solidification furnace. The temperature gradient of the furnace between zones of 1370 and 1330 ℃, corresponding approximately to the solidification temperature of $La_{(1-x)/3}Li_xNbO_3$, for compositions $x = 0.04$, was 8.2 to 12.5 ℃/cm. The crucible was pulled down at a rate of 0.75 mm/h from the 1350 ℃ zone to the 1300 ℃ zone, and then at a rate of 12 ℃/h from the 1300 ℃ zone to room temperature.

2.2. X-ray diffraction (XRD)

Powder XRD measurements of the LNO and LLNO4 samples were performed with Cu Kα radiation using a Rint2000 (Rigaku, Tokyo, Japan) diffractometer equipped with a monochromator, operating at 40 kV and 300 mA.

2.3. Microscopy

Specimens for TEM/STEM observations were prepared by depositing powders on a Cu grid after grinding the bulk single-crystal samples. A conventional 300 kV JEM-3000F microscope (JEOL Ltd.) was used for SAED observations. A 200 kV JEM-2100F microscope (JEOL Ltd.) equipped with a spherical-aberration corrector (CEOS GmbH), enabling structures to be probed with sub-angstrom resolution, was utilised for HAADF/ABF(STEM) imaging. A convergence angle of 25 mrad and a dwell time of 20 μs, together with annular dark-field detector inner/outer angles of 70/240 mrad and annular bright-field detector inner/outer angles of 9/25 mrad, were chosen for HAADF and ABF imaging, respectively. EELS analysis was carried out using a JEM-ARM200F microscope (JEOL Ltd.) equipped with a spherical-aberration corrector (CEOS GmbH), a Gatan Image Filter (GIF) and a Wien-filter type monochromator. The microscope was installed in a room designed and constructed to minimise AC magnetic fields, floor vibrations, air flow volume, temperature fluctuations and acoustic vibrations to provide a stable environment for TEM/STEM analysis. An accelerating voltage of 120 kV and an entrance aperture of 2.5 mm were used. Electron energy-loss spectra were recorded with a parallel beam in TEM mode, using 0.1 eV/channel and an integration time of 1 s per read-out, and an energy resolution of 0.3 eV for all edges. The energy resolution was determined by measuring the full-width half-maximum (FWHM) of the zero-loss peak.

3. Results and discussion

3.1. Composition and crystal symmetry

XRD analysis confirmed that both samples were successfully prepared as pure phases. In agreement with previous reports,[5,9] both the LNO and LLNO4 compounds have orthorhombic crystal structures, as indicated by splitting of the (200) peak (Fig. S1†). Calculation of the lattice constants (see Supplementary Information) revealed that the crystal structure of LLNO4 has a slightly smaller cell volume (0.4825 nm^3) than LNO (0.4864 nm^3). The compositions of the samples were determined by ICP measurements to be $La_{0.33}NbO_3$ and $La_{0.31}Li_{0.04}NbO_3$.

Fig. 2 shows simulated and experimental SAED patterns for LNO and LLNO4 projected along different zone axes. The simulated patterns in Fig. 2a and 2b show that the average crystal structure model of LNO produces only basic spots for zone axes $[001]_p$ and $[110]_p$, respectively. Comparison with the experimental images shows that the additional superlattice reflections {ξ} at (h/2 k/2 0) (h, k = odd numbers) and diffuse satellite reflections {$\boldsymbol{\pi_1}$} at odd multiples of $1/7d^*(110)_p$ and $1/4d^*(001)_p$ in Fig. 2c and 2d (as labelled), respectively, are not reproduced. Careful examination also reveals diffuse reflections {$\boldsymbol{\pi_2}$} with very weak contrast at (n ± 1/3.5)$d^*(110)_p$ (n = integers) and multiples of $1/2d^*(001)_p$, as indicated by a white arrow in Fig. 2d.

Similar differences between the simulated (Fig. S2†) and experimental patterns for LLNO4 (Fig. 2e and 2f) were also observed. Interestingly, the (h/2 k/2 0) reflections in Fig. 2c are replaced by a cluster of four diffuse rods {ξ'} that are aligned parallel to $g(100)_p$ and $g(010)_p$ in the case of LLNO4 (Fig. 2e). The satellite reflections {$\boldsymbol{\pi_1}$'} correspond to a slightly smaller reciprocal spacing of $1/7.3d^*(110)_p$ than that of LNO ($1/7.0d^*(110)_p$). Also, diffuse reflections {$\boldsymbol{\pi_2}$'} at (n ± 1/3.6)$d^*(110)_p$ (n = integer) and multiples of $1/2d^*(001)_p$ were observed with much brighter and sharper contrast (Fig. 2f).

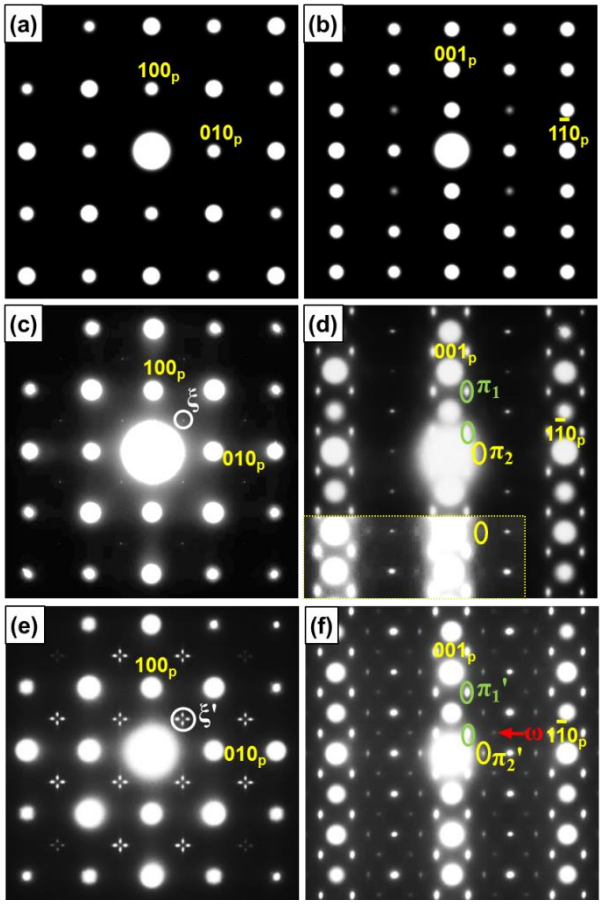

Fig. 2 Selected area electron diffraction (SAED) patterns. Simulated (a) $[001]_p$ and (b) $[110]_p$ patterns and experimental (c) $[001]_p$ and (d) $[110]_p$ patterns for $La_{0.33}NbO_3$ (x = 0, LNO). Experimental (e) $[001]_p$ and (f) $[110]_p$ patterns for $La_{0.32}Li_{0.04}NbO_3$ (x = 0.04, LLNO4). Crystal structure models derived from XRD measurements[18] and a crystal thickness of 10 nm were used in the SAED simulations. A pattern with optimized brightness to highlight the weak diffuse reflections {π_2} is included as an inset in (d).

Additional weak satellite reflections {**ω**} at odd multiples of $1/4d^*(001)_p$ and $(1/2 \pm 1/7.3)d^*(110)_p$, arrowed in red, are also apparent in Fig. 2f. Intensity-scan profiles showing the positions of these weak reflections in greater detail can be found in Fig. S3†.

These results show that the simple crystal structure models obtained from diffraction measurements do not adequately describe the variation in crystal environments in $La_{(1-x)/3}Li_xNbO_3$ materials. Furthermore, replacing La with even a small amount of Li can alter the modulated structure of LNO significantly. In the next section, we describe the local crystal structures in the two compounds by correlating the reciprocal-space SAED results with real-space STEM observations.

3.2. Local crystal structures

3.2.1. $[110]_p$ zone-axis observations

Fig. 3a and 3b show Z-contrast HAADF micrographs taken along the $[110]_p$ zone axes of LNO and LLNO4, respectively.

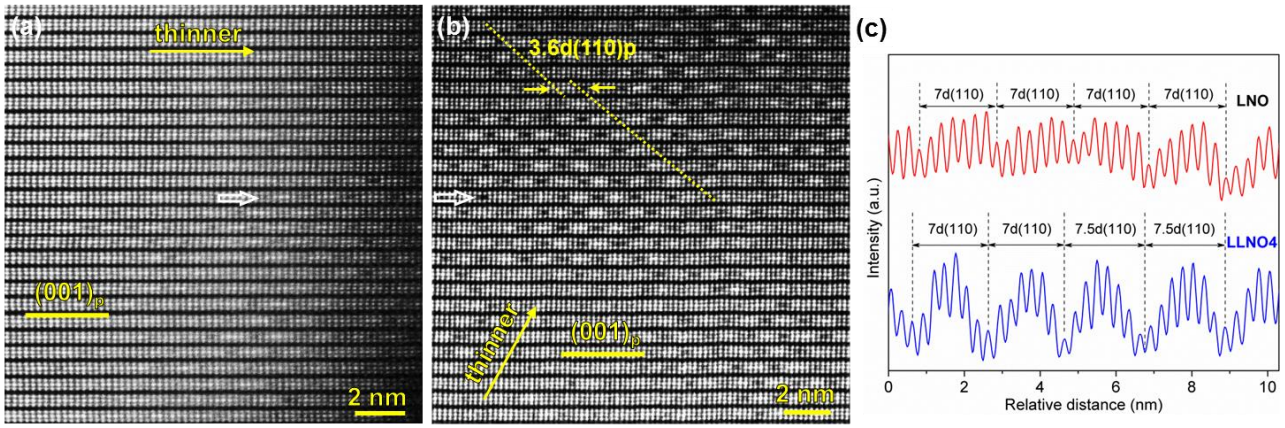

Fig. 3 Medium-magnification HAADF observations. Raw HAADF micrographs taken of (a) LNO and (b) LLNO4 along their $[110]_p$ zone axes. (c) Intensity-scan profiles taken from the arrowed La1 columns in (a) and (b). The dotted lines connecting the darkest La columns in adjacent La1 layers are added in (b) to indicate the lattice shift of two neighbouring microdomains.

The micrographs were taken from thin specimen regions. Only the columns of heavier Nb (Z = 41) and La (Z = 57) atoms display bright contrast, while the weakly scattering Li (Z = 3) and O (Z = 8) atoms produce negligible contrast and are not visible. No La atoms are discernible in the A2 layers, consistent with earlier XRD results.[27] The hollow arrows in Fig. 3a and 3b indicate periodic variations in the La+O+vacancy column contrast in A1 layers along the $[1\text{-}10]_p$ direction in both compounds. In the LNO sample this modulation is only visible in thin regions, unlike in LLNO4, where it is visible over a wider range of sample thicknesses.

The periodic structural variations are more apparent in the intensity-scan profiles in Fig. 3c. A sinusoidal variation of La1 column intensities, directly related to the La occupancies of each column along the $[1\text{-}10]_p$ zone axis, is evident in LLNO4, with superperiodicities of either $7d(110)_p$ or $7.5d(110)_p$. Closer analysis reveals that the two periodicities occur over comparable areas and are randomly arranged to give an average superperiodicity of approximately $7.3d(110)_p$. This sinusoidal distribution of La atoms can be ascribed to a secondary modulated column-ordering of La atoms and vacancies on *A* sites, in addition to the primary La/vacancy partitioning perpendicular to $(001)_p$. A similar distribution of La atoms was also observed in the LNO specimen, although the superperiodicity of the column ordering in LNO of $7d(110)_p$, was at the lower end of the range for LLNO4. In addition, the variation in La column contrast is much smaller, especially in relatively thick regions. This suggests that the ordering of La1 columns is enhanced in LLNO4. It is worth noting that the observed superperiodicities match well with the diffuse satellite reflections $\{\boldsymbol{\pi_1}'\}$ at odd multiples of $1/7.3d^*(110)_p$ for LLNO4 and $\{\boldsymbol{\pi_1}\}$ at odd multiples of $1/7d^*(110)_p$ for LNO in the SAED patterns (Fig. 2d and 2f, respectively).

On the other hand, column ordering appears to be a short-range feature because the periodicities in both compounds are limited in extent. This results in the formation of microdomains (regions within which the column ordering occurs) with irregular shapes and sizes, as seen in the medium-magnification HAADF images in Fig. 3. Microdomain sizes in the HAADF images were measured to be about 10 nm^2 and 30~60 nm^2 for LNO and LLNO4, respectively. More interestingly, a relative lattice shift of approximately $3.6d(110)_p$ (i.e., half the column-ordering periodicity) along the $[1\text{-}10]_p$ direction was found between neighbouring microdomains; an example of this is indicated by the two parallel dotted lines connecting the darkest La columns in adjacent La1 layers in Fig. 3b. This, together with the irregular microdomain morphologies, results in the overlap of microdomains down the zone axis so that La-rich and La-poor columns down $[1\text{-}10]_p$ also overlap, reducing the difference in contrast between different La1 columns in relatively thick crystal regions and regions next to domain boundaries. This is more prevalent in the case of LNO because the microdomains are smaller. The lack of sharp domain boundaries in both compounds can be contrasted with the straight 90 ° rotation domain boundaries observed in cation-deficient perovskite LLTO.[33]

Fig. 4 shows simultaneous high-magnification HAADF and ABF micrographs of LNO and LLNO4 in which the arrangements of $[110]_p$ atom columns within a single microdomain can be discerned. The HAADF images (Fig. 4a and 4c for LNO and LLNO4, respectively) reveal that La columns in the La-rich (La1) layers are quasi-ordered, with columns of similar atom densities in adjacent layers related by a lattice shift of about half the column-ordering periodicity along $[1\text{-}10]_p$ in both materials. Such a shift is consistent with the presence of diffuse reflections, indicated by white arrows in Fig. 2d and 2f, in both materials.

The relatively brighter and sharper contrast of the reflections in LLNO4 can be ascribed to the enhanced column ordering of La atoms and vacancies on *A* sites. The modulated superstructure within a single domain of LNO and LLNO4 observed in the micrographs can be described by unit cells of dimensions ($\sim 3.5\sqrt{2}a_p \times \sim 3.5\sqrt{2}b_p \times 4c_p$) and ($\sim 3.7\sqrt{2}a_p \times \sim 3.7\sqrt{2}b_p \times 4c_p$), respectively; typical supercells are demarcated by dashed rectangles in Fig. 4. A schematic diagram of such a supercell is given in Fig. 7 to show (representative) La and Nb cation configurations and column densities in the case of LLNO4.

In the ABF images in Fig. 4b and 4d, columns of all atoms are visible. The modulated displacements of Nb and O atoms can be seen to vary in magnitude and direction in response to ordering of La1 (La+vacancy[+Li]) columns in both. In perovskites, the displacement of *B* cations and O anions can be attributed primarily to differences in the strengths of their electrostatic interactions with surrounding *A* cations in response to changes in *A*-cation vacancy concentrations. In the case of

LNO and LLNO, these displacements are related to the variation in number densities and hence distributions of surrounding La atoms resulting from the crystal structure modulation. In other words, the degree and direction of Nb/O displacements (and hence varying degrees of $[NbO_6]$ octahedral tilting and distortion) depend on the nature of the ordering (or lack thereof) of La atoms. Indeed, careful examination of the ABF images reveals that LLNO4 contains a greater degree of Nb/O displacements than LNO. This can be more clearly discerned from intensity-scan profiles (Fig. 4e) of La+O+vacancy[+Li] and Nb columns taken across the rectangular areas marked in yellow in the HAADF images of Fig. 4a and 4c. The profiles show that the distance between the La columns with the highest occupancies and adjacent Nb columns (*d*1 for LNO, and *d*1' for LLNO4 in Fig. 4e) is larger than that between columns with the lowest La occupancies and their adjacent Nb columns (*d*2 for LNO, and *d*2' for LLNO4 in Fig. 4e), i.e., $d1 > d2$, and $d1' > d2'$. In addition, $d1' > d1$, $d2' < d2$, and $(d1\text{-}d2)/d2 \approx 11\%$ for LNO, which is approximately half the value of $(d1'\text{-}d2')/d2' \approx 20\%$ for LLNO4. These changes are consistent with the observation of enhanced ordering of La columns, creating a more strongly varied energy surface within La-rich layers in LLNO4.

3.2.2. $[100]_p$/$[010]_p$ and $[001]_p$ zone-axis observations

Fig. 5 shows LNO and LLNO4 modulated structures observed simultaneously by HAADF and ABF along their $[100]_p$ zone axes (viewing down $[100]_p$ allows both La (La+vacancy) and O columns to be distinguished). It should be noted that the $[100]_p$ and $[010]_p$ zone axes are essentially indistinguishable because, despite having orthorhombic symmetry, the differences between *a* and *b* lattice parameters in both LNO and LLNO4 are very small, and the layered perovskite structure is the same in both directions. As indicated by the overlaid structure models, the Nb columns in LNO (actually Nb+O columns, but the O atoms produce negligible contrast in the HAADF image) display suborbicular projections (Fig. 5a). In contrast, elliptical Nb projections with their long diagonals oblique to the $(1\text{-}10)_p$ plane (indicated by the dashed line) were observed in the case of LLNO4 (Fig. 5c). The presence of elliptical Nb projections can be attributed to the channelling of the electron beam when positioned over Nb columns that are subjected to enhanced modulation effects from partial ordering of La within the La1 layers. In contrast, the La-vacancy projections have similar (rounded) shapes in the HAADF images. ABF observations also reveal greater $[NbO_6]$ octahedral tilting/distortion in LLNO4 (Fig. 5d) than in LNO (Fig. 5b). This is consistent with the enhanced modulation of Nb/O columns in LLNO4 mentioned above.

The origin of the splitting of the (h/2 k/2 0) reflections {ξ'} into crosses in the $[001]_p$ SAED pattern was attributed by Garc á-Mart ń et al.[24] to formation of microdomains in which the $[NbO_6]$ octahedra tilts around the $[110]_p$ and $[1\text{-}10]_p$ axes are twinned across intersecting $g(100)_p$ and $g(010)_p$ domain boundaries. However, no direct evidence for the microdomains was provided. In practice it is very difficult to detect such a local twinning of tilting octahedra, even using atomic-resolution HAADF/ABF imaging (Fig. S4†). This is mainly due to the modulated displacements of O atoms in three dimensional space, resulting in only the average column positions being imaged (unfortunately identifying and imaging an extremely thin specimen region with only a single layer of O atoms, which would overcome this problem, is extremely difficult even with state-of-the-art equipment). In fact, the

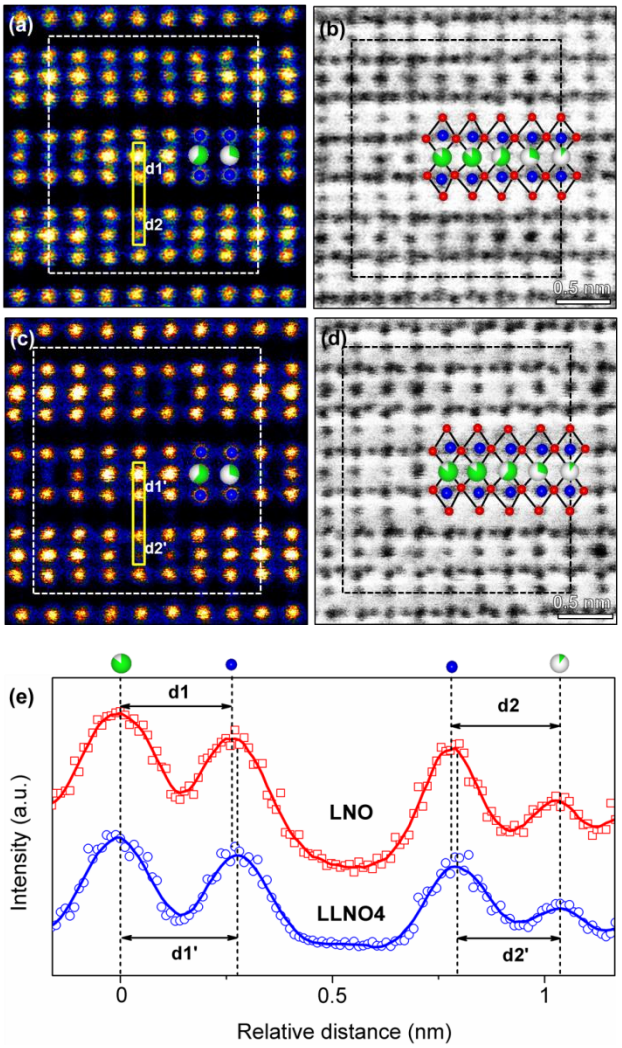

Fig. 4 $[110]_p$ zone-axis HAADF/ABF imaging. (a) HAADF and (b) ABF micrographs of LNO. (c) HAADF and (d) ABF micrographs of LLNO4. Structure model overlays are shown to indicate the positions of O (red), Nb (blue) and La+vacancy+O (green and white) columns. For the latter, the amount of green indicates approximate La column densities. (e) Intensity-scan profiles of neighbouring La+vacancy+O and Nb columns within the solid yellow rectangles in (a) and (c). Supercells of the modulated structure are demarcated by dashed white/black rectangles.

cross-like reflections were also observed in similarly modulated *A*-cation deficient perovskite-related phases, such as $ThNbO_3$[16] and $La_{2/3-x}Li_xTiO_3$.[26,33]

It has been shown that these crosses are a result of a number of features, including microdomains, octahedral tilting, ordering of *A* cations and vacancies.[16,17,21-26] All these features were observed in our LNO and LLNO samples. Although the present results do not permit the origin of the cross-like reflections to be identified with absolute certainty, they strongly suggest that they are produced by enhanced La1 intracolumn ordering when Li is substituted for La in LLNO.

3.3. Chemical bonding: EELS characterization

High-energy-resolution (~0.3 eV) monochromated EELS analysis was carried out to determine the effects of Li

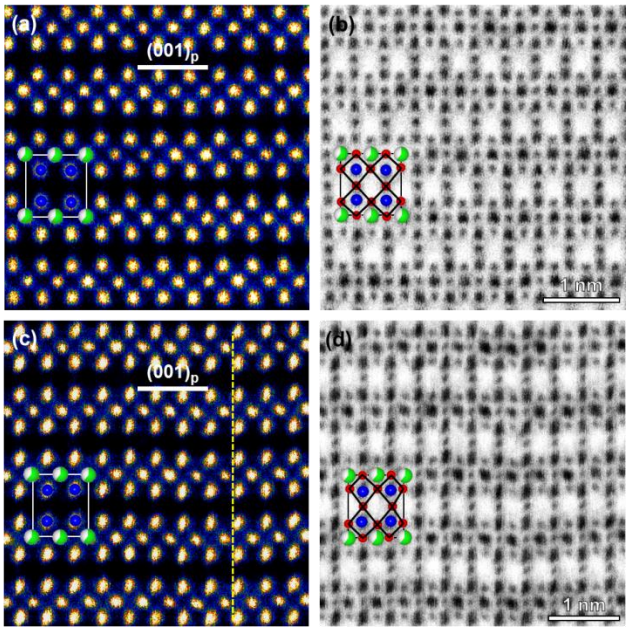

Fig. 5 $[100]_p$ zone-axis HAADF/ABF imaging. (a) HAADF and (b) ABF micrographs of LNO. (c) HAADF and (d) ABF micrographs of LLNO4. The dashed line in (c) indicates the $(1\text{-}10)_p$ plane. Structure model overlays are shown to indicate the positions of O (red), Nb (blue) and La+vacancy (green and white) columns.

substitution on each element's bonding state in LLNO4. Fig. 6 shows the background-subtracted O-*K*, La-$N_{4,5}$, and Nb-$M_{4,5}$ energy-loss near-edge structures (ELNESs) obtained from LNO and LLNO4 samples. All the EELS spectra were obtained from thin specimen regions in parallel-beam (TEM) mode. Although attempts were made to obtain a distinct Li-*K* edge, the low Li content in LLNO4 and the poor scattering power of Li (Z = 3) produced only a weak Li-*K* edge signal which overlaps with the *M* edges of the heavier La and Nb atoms and thus could not be distinguished.

Fig. 6a shows that the O-*K* edge has a slightly smaller pre-peak in LNO than in LLNO4, as indicated by the dotted lines. Generally speaking, in transition metal (TM) oxides the pre-peak originates from transitions to O-2*p* states hybridised with the narrow TM-3*d* band, and is extremely sensitive to TM-O bonding features.[38] XRD measurements have shown that the crystal structure of LLNO4 has a smaller cell volume (0.4825 nm^3) than LNO (0.4864 nm^3), with a slightly smaller average Nb-O bond length in LLNO4 than in LNO. This is consistent with a previous XRD study which showed that cell volumes and average Nb-O bond lengths in LLNO decrease with increasing Li content (for $0 \leq x \leq 0.10$).[9] The slightly greater intensity of the O-*K* prepeak in LLNO4 can be interpreted as a greater amount of Nb-O hybridization (decreased Nb-O bond length) caused by Li substitution. In contrast, no obvious difference between the two compounds can be seen for La-$N_{4,5}$ and Nb-$M_{4,5}$ fine structures. This suggests that Li substitution in LNO, at least in small concentrations, does not significantly affect the bonding states of La and Nb.

3.4. Li positions

ABF imaging along either the $[110]_p$ or the $[100]_p/[010]_p$ zone axes of LLNO4 (Fig. 4d and 5d, respectively) did not reveal any Li columns on or near O4 window sites or vacant *A* sites in the La2 layer. This suggests that Li atoms likely occupy the vacant *A*-site cages in the La1 $(001)_p$ layer, rendering them "invisible" because they are present in the same columns as the high-contrast La atoms. This is consistent with previous XRD studies of $La_{(1-x)/3}Li_xNbO_3$ which found that Li atoms preferentially occupy vacant *A* sites in the La1 layers for composition range x = 0~0.25.[9] Furthermore, La-vacancy ordering should also affect the distribution of Li atoms within this layer. We thus propose that Li atoms preferentially occupy the La-poor columns (as observed from the $[110]_p$ direction) in the La1 layer, since more vacant *A* sites will be available with less electrostatic interactions from neighbouring La atoms. This means that Li atoms should adopt an ordered distribution with a similar superperiodicity, about $7.3d^*(110)_p$, to La. Partial ordering of Li ions in this way may counter the uneven charge distributions induced by column ordering of La atoms, and may also account for the weak satellite reflections {**ω**} at odd multiples of $1/4d^*(001)_p$ and $(1/2 \pm 1/7.3)d^*(110)_p$ in Fig. 2f.

3.5. Cation ordering and Li-ion pathways/mobility

The Li-ion mobility in *A*-cation-deficient perovskites is known to be strongly influenced by the distribution of *A* cations (vacancies), which, because of their large size and charge, block Li migration paths and reduce the space at the bottlenecks (O4 windows formed by four vertex-sharing $[BO_6]$ octahedra) through which Li ions must pass when undergoing long-range migration.[40,41] The higher concentration of *A*-site vacancies in LLNO than in LLTO (to maintain charge balance with the higher charge Nb^{5+} cation compared with Ti^{4+}) would normally be expected to favour higher Li-ion mobility and hence higher ionic conductivity. However, experimentally the Li-ion conductivity of LLNO is found to be roughly one order of magnitude lower than that of LLTO.[4,9,28]

Previous XRD and STEM studies have shown that Li atoms are located within both La1 and La2 layers in LLTO, and Li migration occurs primarily within the La2 layers where a large number of pathways (*A*-site vacancies) are available with relatively open bottlenecks.[10,15] In the case of LLNO, however, our HAADF and ABF observations confirm that both Li and La atoms are confined to the A1 layer, leaving the A2 sites empty, for low Li contents, in agreement with previous reports.[42] In LLNbO, the higher cation vacancy concentration results in a quasi-periodic ordering (structure modulation) which is absent in LLTO. The modulated structure is likely a response to the considerable changes in local bonding resulting from the large difference in ion radii (1.16 Å versus 0.82 Å in 8-fold coordination, respectively) and charge (+3 versus +1, respectively) between La^{3+} and Li^+ in the A1 layer, and the different degrees of tilting and distortion of the high-valent NbO_6 octahedra these induce. In general, (quasi-)ordering of a sublattice restricts ion mobility (e.g., oxide-ion conductivity in brownmillerite-structure versus disordered perovskite-structured oxides[43]) because of greater trapping in local potential wells, so that the modulated structure is likely an impediment to high Li-ion conductivity in this material.

Confinement of Li to the A1 layer will be further consolidated by the modulated displacements of Nb atoms and decrease in lattice volume with increasing Li content, which produce narrower bottlenecks (and thus higher migration

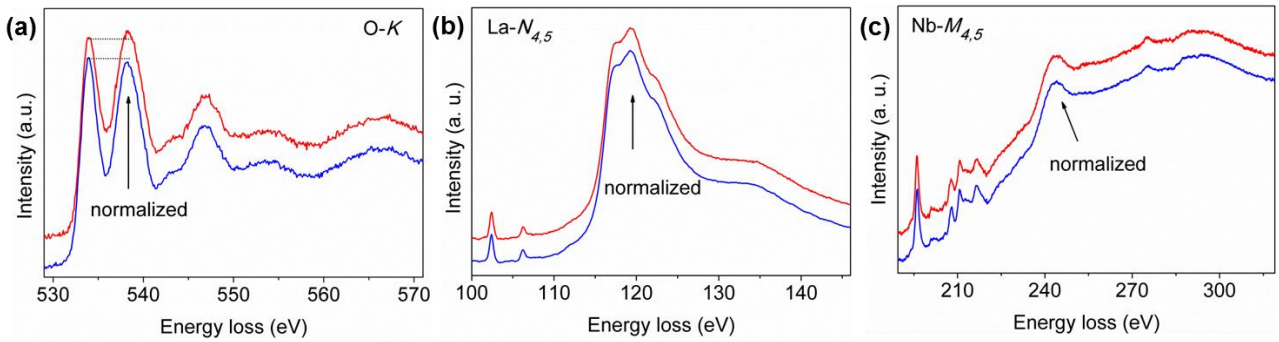

Fig. 6 EELS (TEM mode) analysis. Background subtracted ELNES profiles of (a) O-*K*, (b) La-$N_{4,5}$ and (c) Nb-$M_{4,5}$ with normalized intensities (arrowed) obtained from the LNO (red) and LLNO4 (blue) single crystals.

energy barriers) that restrict movement of Li ions between layers. Fig. 7 summarizes the possible migration pathways in LLNO, as well as their relative importance, taking into account these factors. In contrast to LLTO, it is likely that Li migration occurs primarily within the La1 layer (at least for low concentrations), with migration across and within A2 layers only playing a minor role. In effect this means that a large number of the intrinsic cation vacancies are unable to contribute to Li-ion migration. This may explain the lower bulk ionic conductivity (σ_b) in LLNO compared with LLTO.

In summary, our results reveal the complexity of microstructures in solid electrolyte $La_{(1-x)/3}Li_xNbO_3$ at the atomic scale through a combination of direct (real-space) sub-angstrom resolution observations of all component elements with electron diffraction (reciprocal-space) analysis. This has enabled many of the features of the modulated structure and their relation to the ionic conductivity to be clarified. The precise arrangements of atoms (and vacancies) within domains or at microdomain boundaries in all three spatial dimensions, however, remains a non-trivial task that still needs to be examined, for example through first-principles calculations. More detailed knowledge of the distribution of La vacancies and Li ions within and between columns should provide a comprehensive description of the complex microstructures in these and related systems that can be used to understand and optimise their Li-ion conductivities.

4. Conclusions

Direct TEM/STEM observations reveal that *A*-cation deficient $La_{(1-x)/3}Li_xNbO_3$ perovskite materials have complex modulated crystal structures with partially ordered distributions of *A* cations and vacancies. This involves a long-range layer-ordering of *A* cations into alternating La/Li-rich and La/Li-free layers parallel to $(001)_p$, and a short-range sinusoidal columnar ordering of *A* cations within the La-rich layers. By combining reciprocal electron diffraction analysis and direct atomic-resolution HAADF/ABF observations, we determined that the crystal structures of $La_{(1-x)/3}Li_xNbO_3$ perovskites where $x = 0$ and 0.04 can be described by supercells of ($\sim 3.5\sqrt{2}a_p \times \sim 3.5\sqrt{2}b_p \times 4c_p$) and ($\sim 3.7\sqrt{2}a_p \times \sim 3.7\sqrt{2}b_p \times 4c_p$), respectively.

Columnar ordering is observed to occur together with modulated displacements of Nb/O atoms within microdomains

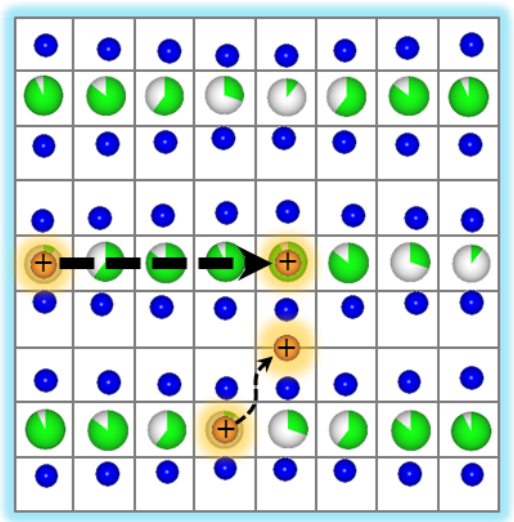

Fig. 7 Schematic diagram showing the La and Nb cation configurations and (approximate) column densities observed down the $[110]_p$ zone axis in the case of LLNO4. The thick/thin arrows indicate possible primary/secondary Li-ion pathways. Nb: blue, Li: orange, La: green, and La-vacancies: white.

of varied shapes and sizes. It was also found that Li substitution for La by even a small amount can lead to significant modifications to the local crystal structure and overall microstructure, with enlarged microdomains and enhanced column ordering producing increased degrees of superperiodicity and incommensurability. At the atomic level, modulated displacements of Nb/O atoms and greater [NbO_6] octahedral tilting/distortion were observed. The combined effects of Li being confined to the A1 layer and *A*-cation columnar ordering are speculated to have a deleterious effect on the Li-ion mobility of this family of materials and may explain the lower ion conductivity of $La_{(1-x)/3}Li_xNbO_3$ compared with $La_{(2-x)/3}Li_xTiO_3$ observed by experiment.

Acknowledgements

Part of this research was supported by the Japan Society for the Promotion of Science (JSPS) through its Funding Program for World-Leading Innovative R&D on Science and Technology (FIRST Program).

Notes and references

[a] Nanostructures Research Laboratory, Japan Fine Ceramics Center, Nagoya 456-8587, Japan. E-mail: gaoxiang@jfcc.or.jp
[b] Faculty of Engineering, Shinshu University, Nagano 380-8553, Japan.
[c] Battery Materials Division, Toyota Motor Corporation, Shizuoka 410-1193, Japan.
[d] Institute of Engineering Innovation, The University of Tokyo, Tokyo 113-8586, Japan. E-mail: ikuhara@sigma.t.u-tokyo.ac.jp
† Electronic Supplementary Information (ESI) available. See DOI: 10.1039/b000000x/

1 P. K. Davies, *Curr. Opin. Solid State Mater. Sci.*, 1999, **4**, 467–471.
2 L. Latie, G. Villeneuve, D. Conte and G. Le Flem, *J. Solid State Chem.*, 1984, **51**, 293–299.
3 A. Nadiri, G. Le Flem and C. Delmas, *J. Solid State Chem.*, 1988, **73**, 338–347.
4 Y. Inaguma, C. Liquan, M. Itoh, T. Nakamura, T. Uchida, H. Ikuta and M. Wakihara, *Solid State Commun.*, 1993, **86**, 689–693.
5 Y. Kawakami, H. Ikuta and M. Wakihara, *J. Solid State Chem.*, 1998, **2**, 206–210.
6 S. García-Martín, J. M. Rojo, H. Tsukamoto, E. Morán and M. A. Alario-Franco, *Solid State Ionics*, 1999, **116**, 11–18.
7 M. Nakayama, K. Imaki, H. Ikuta, Y. Uchimoto and M. Wakihara, *J. Phys. Chem. B*, 2002, **106**, 6437–6441.
8 M. Nakayama, K. Imaki, W. Ra, H. Ikuta, Y. Uchimoto and M. Wakihara, *Chem. Mater.*, 2003, **15**, 1728–1733.
9 A. Belous, E. Pashkova, O. Gavrilenko, O. V'yunov and L. Kovalenko, *Ionics*, 2003, **9**, 21–27.
10 S. Stramare, V. Thangadurai and W. Weppner, *Chem. Mater.*, 2003, **15**, 3974–3990.
11 A. G. Belous, O. N. Gavrilenko, S. D. Kobilyanskaya, O. I. V'Yunov, V. V. Trachevskii and O. Bohnke, *Chem. Met. Alloys*, 2010, **3**, 90–95.
12 M. Nakayama, J. Shirakawa and M. Wakihara, *Solid State Ionics*, 2006, **177**, 1259–1266.
13 J. F. Ihlefeld, P. G. Clem, B. L. Doyle, P. G. Kotula, K. R. Fenton and C. A. Apblett, *Adv. Mater.*, 2011, **23**, 5663–5667.
14 M. Catti, *J. Phys. Chem. C*, 2008, 12, 11068–11074.
15 X. Gao, C. A. J. Fisher, T. Kimura, Y. H. Ikuhara, H. Moriwake, A. Kuwabara, H. Oki, T. Tojigamori, R. Huang and Y. Ikuhara, *Chem. Mater.*, 2013, **25**, 1607–1614.
16 M. A. Alario-Franco, I. E. Grey, J. C. Joubert, H. Vincent, and M. Labeu, *Acta Cryst.*, 1982, **A38**, 177–186.
17 G. X. Wang, P. Yao, D. H. Bradhurst, S. X. Dou, and H. K. Liu, *Solid State Ionics*, 1999, **124**, 37–43.
18 R. A. Dilanian, A. Yamamoto, F. Izumi and T. Kamiyama, *Mol. Cryst. Liq. Cryst.*, 2000, **341**, 225–230.
19 G. King and P. M. Woodward, *J. Mater. Chem.*, 2010, **20**, 5785–5796.
20 B. S. Guiton and P. K. Davies, *Nature Mater.*, 2007, **6**, 586–591.
21 M. Labeu, I. E. Grey, J. C. Joubert, H. Vincent and M. A. Alario-Franco, *Acta Cryst.*, 1982, **A38**, 753–761.
22 M. Labeu, I. E. Grey, J. C. Joubert, J. Chenevas, A. Collomb and J. C. Guitel, *Acta Cryst.*, 1985, **B41**, 33–41.
23 S. García-Martín, F. García-Alvarado, A. D. Robertson, A. R. West and M. A. Alario-Franco, *J. Solid State Chem.*, 1997, **128**, 97–101.
24 S. García-Martín and M. Á. Alario-Franco, *J. Solid State Chem.*, 1999, **148**, 93–99.
25 K. Kishida, K. Goto and I. Haruyuki, *Acta Cryst.*, 2009, **B65**, 405–415.
26 J. L. Fourquet, H. Duroy and M. P. Crosnier-Lopez, *J. Solid State Chem.*, 1996, **127**, 283–294.
27 J. Emery, O. Bohnke, P. Florian and K. Marzouk, *J. Phys. Chem. B*, 2005, **109**, 20680–20689.
28 Y. Inaguma and M. Nakashima, *J. Power Sources*, 2013, **228**, 250–255.
29 Y. Kawakami, H. Ikuta and M. Wakihara, *J. Solid State Electrochem.*, 1998, **2**, 206–210.
30 M. Nakayama, H. Ikuta, Y. Uchimoto and M. Wakihara, *Appl. Phys. Lett.*, 2004, **84**, 4227–4229.
31 S. D. Findlay, N. Shibata, H. Sawada, E. Okunishi, Y. Kondo and T. Yamamoto, *Appl. Phys. Lett.*, 2009, **95**, 191913.
32 S. D. Findlay, N. Shibata, H. Sawada, E. Okunishi, Y. Kondo and Y. Ikuhara, *Ultramicroscopy*, 2010, **110**, 903–923.
33 X. Gao, C. A. J. Fisher, T. Kimura, Y. H. Ikuhara, A. Kuwabara, H. Moriwake, H. Oki, T. Tojigamori, K. Kohama and Y. Ikuhara, *J. Mater. Chem. A*, 2014, **2**, 843–852.
34 R. Huang, Y. H. Ikuhara, T. Mizoguchi, S. D. Findlay, A. Kuwabara, C. A. J. Fisher, H. Moriwake, H. Oki, T. Hirayama and Y. Ikuhara, *Angew. Chem. Int. Ed.*, 2011, **50**, 3053–3057.
35 X. Gao, Y. H. Ikuhara, C. A. J. Fisher, H. Moriwake, A. Kuwabara, H. Oki, K. Kohama, R. Yoshida, R. Huang and Y. Ikuhara, *Adv. Mater. Interfaces*, 2014, **1**, 1400143.
36 S. J. Zheng, C. A. J. Fisher, T. Hitosugi, A. Kumatani, S. Shiraki, Y. H. Ikuhra, A. Kuwabara, H. Moriwake, H. Oki and Y. Ikuhara, *Acta Mater.*, 2013, **61**, 7671–7678.
37 H. Moriwake, A. Kuwabara, C. A. J. Fisher, R. Huang, T. Hitosugi, Y. H. Ikuhara, H. Oki and Y. Ikuhara, *Adv. Mater.*, 2013, **25**, 618–622.
38 H. Kurata, E. Lefévre and C. Colliex, *Phys. Rev. B*, 1993, **47**, 13763–13768.
39 K. Kudo, K. Kakiuchi, K. Mizutani, T. Fukami and K. Hoshikawa, *J. Crystal Growth*, 2014, **267**, 150–155.
40 K. Moria, S. Tomihira, K. Iwase, T. Fukunaga, *Solid State Ionics*, 2014, **268**, 76-81.
41 H. Moriwake, X. Gao, A. Kuwabara, C. A. J. Fisher, T. Kimura, Y. H. Ikuhara, K. Kohama, T. Tojigamori and Y. Ikuhara, *J. Power Sources*, 2015, **276**, 203-207.
42 A. Belous, E. Pashkova, O. Gavrilenko, O. V'yunov and L. Kovalenko, *J. Euro. Ceram. Soc.*, 2004, **24**, 1301–1304.
43 J. E. Auckett, A. J. Studer, E. Pellegrini, J. Ollivier, M. R. Johnson, H. Schober, W. Miiller and C. D. Ling, *Chem. Mater.*, 2013, 25, 3080−3087.

Table of Contents Entry:

Atomic-resolution STEM reveals complex ordering of A-site cations and vacancies, as well as NbO_6 octahedral tilting and distortion, in Li-conducting perovskites $La_{(1-x)/3}Li_xNbO_3$.